Acta Biomaterialia 64 (2017) 1–14

Contents lists available at ScienceDirect

Acta Biomaterialia

journal homepage: www.elsevier.com/locate/actabiomat

Full length article

Hierarchical structure and compressive deformation mechanisms of bighorn sheep (*Ovis canadensis*) horn

Wei Huang [a,1], Alireza Zaheri [b,1], Jae-Young Jung [a], Horacio D. Espinosa [b,c,*], Joanna Mckittrick [a,d,*]

[a] Materials Science and Engineering Program, University of California, San Diego, La Jolla, CA 92037, USA
[b] Theoretical and Applied Mechanics Program, Northwestern University, Evanston, IL 60062, USA
[c] Department of Mechanical Engineering, Northwestern University, Evanston, IL 60062, USA
[d] Department of Mechanical and Aerospace Engineering, University of California, San Diego, La Jolla, CA 92037, USA

ARTICLE INFO

Article history:
Received 14 May 2017
Received in revised form 21 September 2017
Accepted 29 September 2017
Available online 30 September 2017

Keywords:
Sheep horn
Keratin cells
Compressive deformation
Impact resistance
Anisotropy

ABSTRACT

Bighorn sheep (*Ovis canadensis*) rams hurl themselves at each other at speeds of ~9 m/s (20 mph) to fight for dominance and mating rights. This necessitates impact resistance and energy absorption mechanisms, which stem from material-structure components in horns. In this study, the material hierarchical structure as well as correlations between the structure and mechanical properties are investigated. The major microstructural elements of horns are found as tubules and cell lamellae, which are oriented with (~30°) angle with respect to each other. The cell lamellae contain keratin cells, in the shape of pancakes, possessing an average thickness of ~2 μm and diameter of ~20–30 μm. The morphology of keratin cells reveals the presence of keratin fibers and intermediate filaments with diameter of ~200 nm and ~12 nm, respectively, parallel to the cell surface. Quasi-static and high strain rate impact experiments, in different loading directions and hydration states, revealed a strong strain rate dependency for both dried and hydrated conditions. A strong anisotropy behavior was observed under impact for the dried state. The results show that the radial direction is the most preferable impact orientation because of its superior energy absorption. Detailed failure mechanisms under the aforementioned conditions are examined by bar impact recovery experiments. Shear banding, buckling of cell lamellae, and delamination in longitudinal and transverse direction were identified as the cause for strain softening under high strain rate impact. While collapse of tubules occurs in both quasi-static and impact tests, in radial and transverse directions, the former leads to more energy absorption and impact resistance.

Statement of Significance

Bighorn sheep (*Ovis canadensis*) horns show remarkable impact resistance and energy absorption when undergoing high speed impact during the intraspecific fights. The present work illustrates the hierarchical structure of bighorn sheep horn at different length scales and investigates the energy dissipation mechanisms under different strain rates, loading orientations and hydration states. These results demonstrate how horn dissipates large amounts of energy, thus provide a new path to fabricate energy absorbent and crashworthiness engineering materials.

1. Introduction

Natural structural materials possess variety of unique self-assembled hierarchical structures which result in remarkable mechanical efficiency, such as resistance to different loading modes and ability to sustain extreme deformations with limited selection of chemical constitutes along with optimized weight [1]. One example is the bighorn sheep (*Ovis canadensis*) horn, which can support an impact force as large as ~3400 N [2]. The velocity of the intraspecific combat between two males can reac h ~9 m/s, deaccelerating in ~2 ms with a deceleration estimated as ~450 g [3]. Hence, sheep horns experience high impact loads during combat with others animals and protection from predators [4]. At the same time, they need to absorb the impact energy to minimize its transmission to the skeletal frame of the animal.

* Corresponding authors at: Theoretical and Applied Mechanics Program, Northwestern University, Evanston, IL 60062, USA (H.D. Espinosa). Materials Science and Engineering Program, University of California, San Diego, La Jolla, CA 92037, USA (J. Mckittrick).
E-mail addresses: espinosa@northwestern.edu (H.D. Espinosa), jmckittrick@eng.ucsd.edu (J. Mckittrick).
[1] These authors contribute equally to the work.

https://doi.org/10.1016/j.actbio.2017.09.043
1742-7061/

Based on the study of sheep collisions, an estimate of the strain rate experience by the horn material is of the order of 10^2–10^3 s^{-1} because of the extremely short impact time (~2 ms) [3], which is much higher than previous reported result (~38 s^{-1}) [5]. The reason of the differences is in latter work, the initial impact speed was set as 4.7 m/s, and the horn shape effects were considered as well. The higher strain rates estimated in the present work are based on the condition of ~9 m/s for the initial impact velocity a nd ~450 g for the acceleration reported by Courtney et.al [3]. This reveals the importance of high impact resistance in these materials. Horns are permanent structures which are made of an external keratin sheath covering a spongy bone core, and will not regenerate or recover once fractured [6,7]. For the efficiency of horn in fighting, they are expected to be: stiff and strong enough to resist the impact force; tough enough to dissipate impact energy without fracture; light enough to be functional [2,8,9]. The overall shape of the horn, as well as the bone tissue inside the horn sheath, plays an important role in protection of the sheep brain from impacts [5]. In this regard, understating the role of structural-material components on mechanical properties of horn keratin sheath provides insight into utilization of these tissues during the lifetime of the animal.

Keratin is selected through the evolutionary process for a plethora of animal tissues, such as hooves, claws, nails, hairs, wools and scales [10,11]. Horn keratin is composed of α-helical crystalline intermediate filaments (IFs, 7–10 nm in diameter), embedded in an amorphous non-helical keratin matrix [12–14]. Keratin in horns contains disulfide bonds as well as secondary bonds, such as hydrogen bonds, to stabilize the amorphous matrix, by holding together the non-crystalline polypeptides [15]. The hydrogen bonds are thought to be sensitive to hydration, which result in mechanical properties dependent on water content [16,17]. Indeed, studies on the effect of hydration revealed a reduction on the stiffness and strength of horn keratin [18–22]. The Young's modulus of bighorn sheep horn has been reported to increase from 0.63 to 2.2 GPa as the water content decreased from 34.5 to 10.6 wt% water content [20]. However, the fracture toughness of oryx horn was found to increase from 2.2 $MPa/m^{1/2}$ in dry condition (0 wt% water content) to 4.5 $MPa/m^{1/2}$ in fresh condition (20 wt% water content) [23]. This was argued as the result of limited matrix yielding and plastic deformation in the fully dry state. The hydration sensitivity for many keratinous materials such as human hair and nails [24,25], feathers [26] and hooves [27] has been reported in the past. It is believed that the sensitivity in general is a result of absorption of water [28] and disruption of hydrogen bonds with the subsequent decrease in the number of effective bonding in the matrix of keratin, which generally decreases the overall strength and stiffness [18]. In conjunction with this, it was reported that the water molecules tend to bind on the hydrophilic sites of protein in both the IFs and amorphous matrix. However, the matrix showed higher capability of binding water molecules than the IFs, thus absorbing more water [29].

Besides hydration sensitivity, anisotropy plays an influential role on the mechanical properties of keratinized materials. McKittrick et al. [20] conducted quasi-static compression tests on different orientations of sheep horn specimens. Three main loading directions in horns were introduced: Longitudinal, which is along the growth direction of the horn; radial, which is the main impact direction in the bighorn sheep horn; transverse, which is another orthogonal direction perpendicular to the growth direction. Smaller elastic modulus and yield strength were found in the radial direction, compared to the longitudinal and transverse directions. They also observed deformation mechanisms such as microbuckling and delamination of lamellae during specimen compression. In another work, Trim et al. [21] investigated the stress-state dependent structure-property relationship under quasi-static compression and tension tests. They found insignificant variation of properties for specimens obtained from the proximal region to the distal region of the horn. They also observed buckling of lamella and shear-type failure mode in compression for longitudinal and transverse orientations, respectively. Recently, Horstemeyer et al. [22] found that as the compressive strain rate increased, the Young's modulus and yield strength were increased for samples in only two orientations (longitudinal and radial). For the case of tensile behavior, Zhang et al. [30] showed higher tensile strength and elastic modulus in the longitudinal direction than the transverse direction of the horns from domestic bovines.

Understanding the aforementioned anisotropic behavior requires the description of the hierarchical structure at different length scales. Fig. 1 shows the previously illustrated hierarchical structure of bighorn sheep horn and equine hoof. Microscopically, most keratinous materials have heterogeneous structures. For the case of horns and hooves, micro-tubules (40–100 μm in diameter) orientated in the longitudinal directions (Fig. 1) are embedded in the intratubular matrix [20,31,32]. Keratin cells (2–5 μm thick) are stacked layer-by-layer forming a lamellar structure around

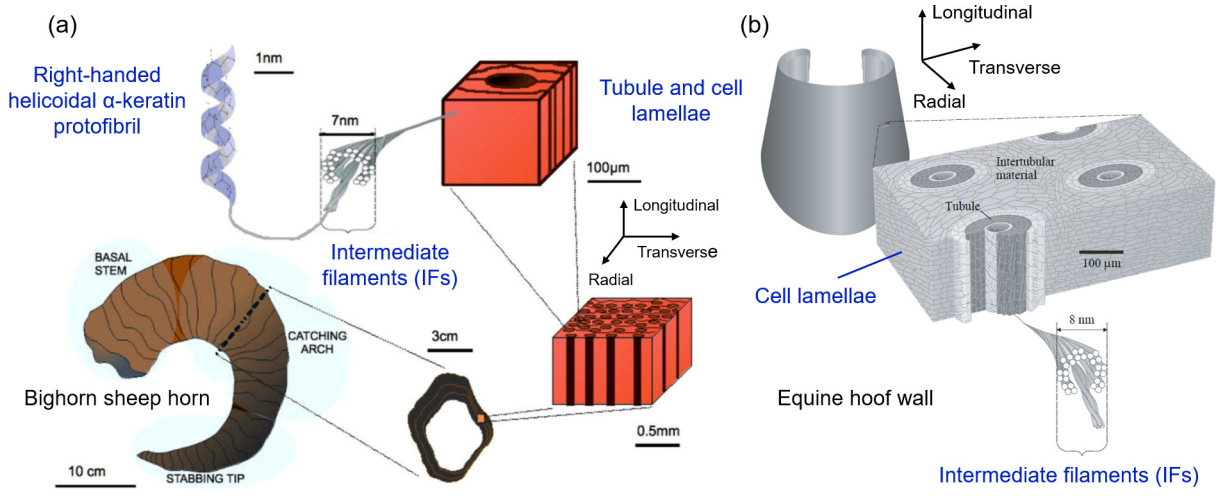

Fig. 1. Hierarchical structure of bighorn sheep horn (a) and equine hoof (b) are adapted from [20,32] respectively. (a) Tubule and cell lamellae were found along the longitudinal direction. Intermediate filaments with a diameter around 7 nm compose the horn keratin. (b) Tubule and intertubular materials were found in equine hoof. Cell lamellae were perpendicular with the tubules. The basic composition is IFs similar as the bighorn sheep horn.

the tubules as well as in the intertubular area. The arrangements of these lamellar cells vary in different tissues and species. Previously, Kasapi and Gosline [31] showed the complex orientation of the IFs around the tubular cortex as well as in the intertubular area of equine hooves. These along with the cell lamellae arrangements were presented as the influential factors on mechanical properties of hooves. However, to the best of our knowledge the keratin cell lamellae arrangements and IFs orientations in the bighorn sheep horn have not previously been identified. Moreover, previous studies were mostly limited to low strain rates ($\sim 10^{-3}\ s^{-1}$) [20,21]. Even though some high-strain-rate mechanical properties were recently reported, deformation mechanisms as a function of strain rates were not sufficiently characterized. We believe this is due to impedance mismatch between the employed bars used in the Kolsky bar experimental setup and the horn samples. This led to a limited understanding of the energy absorption mechanisms [22]. Moreover, understanding of the mechanical behavior was limited by the lack of knowledge of the keratin microstructure. Thus, the present work aims to understand the following points: 1) The hierarchical structure of bighorn sheep horn, including tubules, cell arrangement, intermediate filaments orientations; 2) The strain rate dependency, anisotropicity, and hydration effects on compressive properties; and 3) The compressive deformation mechanisms and their correlation with the hierarchical structure.

2. Experiments and methods

Two horns of different bighorn sheep (*Ovis canadensis*) from the Rocky Mountain area were purchased from the Wilderness Trading Company (Pinedale, WY), and were kept at room temperature in a dry environment, as shown in Fig. 2a. The total lengths of horns a re ~60 cm, with diameters ~9 cm at the proximal region. Based on the length of the horns, they are estimated to be 6–8 years old. However, the time between the harvesting of horns and our tests remains unknown. A section near the base of the original horn was cut, showing a hollow interior (Fig. 2b). The thickness of the horn sheath in Fig. 2b changes with the position through the cross section. The outer impact surface has a thickness ~2–3 cm, while the inner is around 1 cm thick. Thus, samples were collected from the thicker area near the proximal region, which is the most probable impact part, to conduct structural characterization and mechanical testing. These samples are assumed to be representative of the whole horn according to previous structural characterization and mechanical results, which indicated no significant difference in density, tensile, and compressive stress-strain behaviors between different locations along the length of the horn [21]. Since the internal regions of the horn are less compromised during impact, they were not investigated in detail in this study. Irregular shapes and closed tubules in the cross sections of horn samples were reported in previous studies [20,21]. We hypothesize this to be the result of accumulated damage from ramming during the bighorn sheep's life. To avoid using damaged regions, in this study specimens were carefully inspected and prepared from pristine regions of the horn to avoid history effects because of apparent ramming damage. Likewise, sample preservation and preparation were optimized to avoid generating imperfections that could impact the characterization and mechanical properties here reported.

2.1. High resolution X-ray micro-computed tomography (HR μ-CT)

Three $2 \times 2 \times 4\ mm^3$ horn samples were cut from the middle part of impact area (Fig. 2b). A 2.5 vol% glutaraldehyde solution was applied to fix the samples for 24 h. After washing for 3 times, 2% osmium tetroxide (OsO_4) was used to stain the specimen for 3 days to increase the contrast. The samples were then washed with deionized (DI) water five times. The microstructure of the outer impact area was evaluated by high resolution X-ray microscopy (XRM, Xradia 510 Versa, Carl Zeiss Microscopy, Pleasanton, CA, USA). The scan parameters employed in the experiment are a tilt increment of 0.15° (for a 360° of rotation angle, a 2401 of tilts) and an isotropic voxel size of 1.95 μm at a 80 kV acceleration voltage. The series of tiff images were reconstructed by Amira software (FEI Visualization Sciences Group, Burlington, MA, USA) with a module of volume rendering. The reconstructed

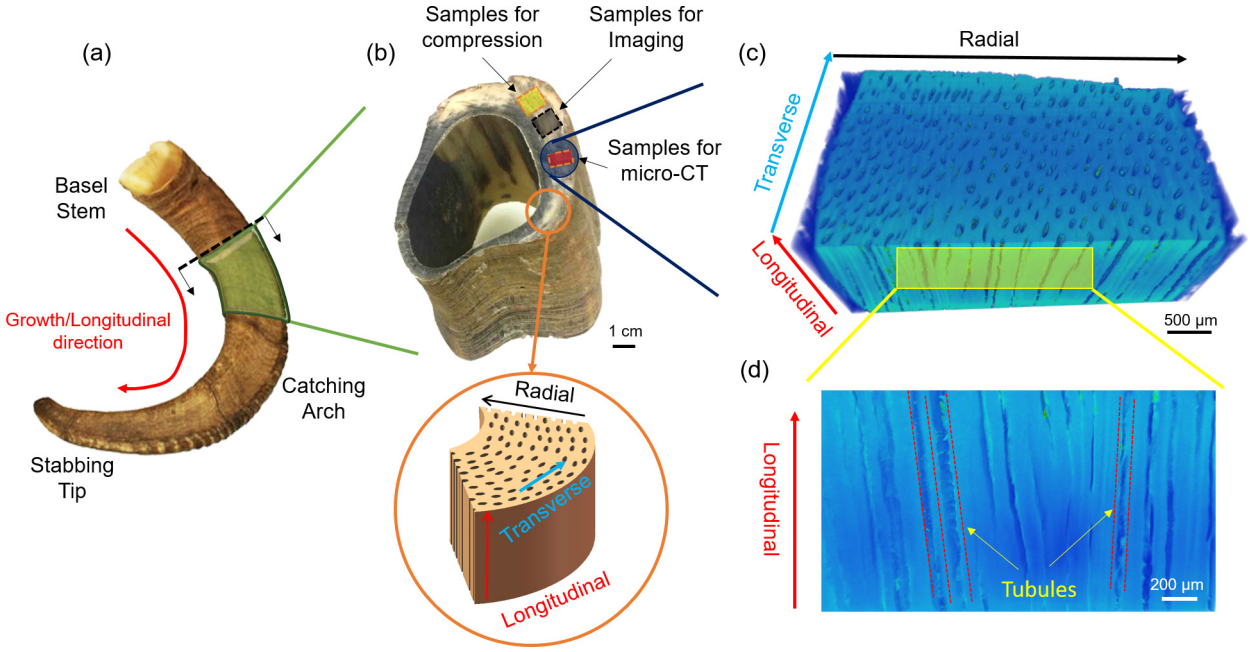

Fig. 2. Bighorn sheep horn specimen and the tubular structure: (a) Photograph of the bighorn sheep horn used for further analysis; (b) Outer keratin sheath with hollow interior. Schematic of the tubules and orientations are shown: Longitudinal direction parallel with the tubules, radial direction along the minor axis of the ellipse shape of tubule cross section, and transverse direction along the major axis of the cross section; (c) High resolution X-ray micro-computed tomography (HR μ-CT) image of horn sample; (d) Longitudinal section from the HR μ-CT image, showing the continuous tubules along the longitudinal direction.

three-dimensional rendering model was cropped and visualized to show both transverse and longitudinal cross-sections. A colormap (from a minimum intensity with a dark blue to a maximum intensity with a red) was applied to distinguish the different keratin densities based on the acquired X-ray intensities.

2.2. Optical and scanning electron microscopy imaging

Samples (six samples in total, three from one horn and three from the second one) were cut into cubes with dimension $4 \times 4 \times 4\ mm^3$ and were located ~5 mm from the impact surface as showed in Fig. 2b. An ultramicrotome was used to make flat surfaces of the cross and longitudinal sections in each block. Differential interference contrast (DIC) optical microscopy images were taken on the flat surface by a Keyence VHX 1000 (Keyence, Palatine, IL, USA). Thin slices (~1 μm thick, 6–9 slices for each cube) were cut by ultramicrotome (Leica EM UC6, Leica Microsystems Inc., Buffalo Grove, IL, USA) and stained with toluidine blue, which increases the contrast of the keratin cells under the optical microscope. Optical microscopy images with different magnification (5×, 10×, 20×, 40×) were acquired. Porosities/pore sizes, cell lamellae angle and cell sizes were quantified from the optical images. Half of the 6 cubes were immersed in a 2.5 vol% glutaraldehyde solution overnight to fix the structure. A graded series of ethanol solutions (20%, 40%, 60%, 80%, 95%, and 100% vol% ethanol) were applied to further dehydrate the samples. Then the samples were freeze-fractured after immersion in liquid nitrogen in both cross and longitudinal directions. Finally, a critical point dryer (Autosamdri-851, Tousimis, Rockville, MD, USA) was used to further remove the excess ethanol. Samples were sputter coated with iridium (Quorum Technologies Ltd., West Sussex, UK) to enhance the sample electron conductivity before performing scanning electron microscopy (SEM) imaging. An ultra-high resolution microscope (FEI, Hillsboro, OR, USA) was applied to conduct the SEM imaging.

2.3. Transmission electron microscopy imaging

Samples (four in total) were cut into small blocks with dimension $2 \times 1 \times 1\ mm^3$ from the similar areas as the SEM samples. Then the samples were immersed in a 2.5 vol% glutaraldehyde solution overnight. 2% OsO_4 was applied to stain the horn specimens. After 24 h of staining at room temperature, the samples were washed with DI water five times. Then the samples were further stained with uranyl acetate for 1 day to obtain better contrast. The samples were washed with DI water for two times and then dehydrated with graded series of ethanol solutions (20%, 50%, 70%, 90% and 100% vol% ethanol). After dehydration, samples were embedded in Spurr's low viscosity resin (Electron Microscopy Sciences, Hatfield, PA, USA). An ultramicrotome (Leica EM UC6, Leica Microsystems Inc., Buffalo Grove, IL, USA) was used to pre pare ~80 nm thin sections to perform further imaging. Sections on copper grids were post-stained by lead citrate solutions to enhance contrast. A FEI Tecnai 12 (Spirit) (80 kV) electron microscope (FEI, Hillsboro, Oregon, USA) was used to image the stained sections with magnification from 1000× to 10,000×. The diameters of macrofibrils and orientations are estimated from TEM images.

2.4. Compression tests

Due to the hollow design of horns, samples used for compression tests were obtained from the proximal and central regions of horn where it is the thickest (Fig. 2b). Samples were taken at positions ~10–20 cm from the proximal region of the horns. The dimensions of the samples for quasi-static and dynamic testing were 4 mm in all directions, which were prepared by use of handsaw and powered-saw with diamond blade. Then, the samples were ground to obtain parallel faces. To examine the anisotropic behavior of horn, samples were cut from three different orientations: longitudinal, transversal and radial as shown in Fig. 2b. The samples were tested in ambient conditions as well as hydrated, in which they were immersed in DI water for 72 h. In the dried condition, the moisture content was around 10%, however, it is increased to ~30 ± 0.7% in the hydrated condition (similar to the ~35% reported in a previous study [20]). At least three samples for each direction, both in the dry and hydration conditions, were tested and the final results were averaged. For the quasi-static uniaxial compression test, a universal testing machine with a 30 kN load cell (Instron 3367 Dual Column Testing Systems, Instron, MA, USA) was used. The specimens were tested at strain rates of $1 \times 10^{-3}\ s^{-1}$, $1 \times 10^{-1}\ s^{-1}$ and $5 \times 10^{-1}\ s^{-1}$ (six samples for each condition). In all experiments, the loading process was continued until fracture occurred. Given that the natural striking rates of sheep horns are $\sim 10^2$–$10^3\ s^{-1}$, a split Hopkinson bar system was employed to test the samples dynamically. This system has been extensively used to determine the high strain rate mechanical properties of many materials from monolithic materials such as metals [33,34], ceramics [35] and polymers [36,37] to composite materials [38,39]. However, in the case of low impedance materials such as biological materials, proper modifications in the split Hopkinson technique are required in order to obtain reliable and accurate results [40]. These mainly include strain rate constancy and stress equilibrium at the interfaces of the sample [41,42]. The key to achieve the aforementioned criteria is the impedance mismatch ratio between bars and the sample [43]. To this end, woven glass/epoxy composite (G-10) rods with a diameter of 12.7 mm were used for striking, incident, and transmission bars. Lower impedance of these bars in compare to the steel and aluminum with the same size (i.e. one fifth of steel and one half of aluminum) leads to optimal strain rate constancy and stress uniformity over the specimen length [41]. Moreover, the higher yield strength of G-10 is an advantage compared to polymeric bars, which provides higher load capacity (i.e., compressive stresses) to crush the specimens. To achieve a linear ramp loading, a polycarbonate pulse shaper was used on the impact side of the incident bar. In the present setup, a gas gun was used to fire the striker bar. A compressive pulse is generated on the incident bar, which travels towards the specimen. A portion of the pulse is transmitted through the transmission bar by the specimen sandwiched between two bars and the remaining is reflected at the incident bar-specimen interface. Finally, the stress pulses in the bars were recorded by strain gages, amplified, and recorded in an oscilloscope. The obtained stress-strain curves for all strain rates are given in Section 3. Due to the cost of experimentation and analysis, compared to the 6 samples tested in compression at low strain rates, three samples were selected as representative in each testing condition. The average strain rate was $\sim 4000\ s^{-1}$.

2.5. Hopkinson bar impact recovery tests and failure surface imaging

To further understand the interplay between horns microstructural features such as tubules and their role in determining the overall compressive deformation behavior, bar impact recovery experiments (i.e., experiments in which the sample deformation is limited to a specific strain level) were conducted. For the quasi-static tests, specimens were loaded to a specified strain level and then unloaded with the same rate to the zero load level. Optical images of different surfaces of the deformed specimens were taken before and after the tests to track changes in microstructure. In the bar impact recovery tests, a stopper ring surrounding the sample was employed [44]. The function of the ring is to carry

the load after the specimen achieves the desired axial strain. The desired strain was set around 25–30% since the softening behavior occurs at that level observed from the obtained stress-strain curves in Fig. 7. The stopper ring was made of G-10 with the same outer diameter as the bars and an inner diameter large enough to avoid any radial confinement of the sample during axial compression. The faces of the ring were prepared to be as parallel as possible to the bar end faces. Depending upon the desired strain level in the recovered samples, the length of the ring was adjusted. It should be noted that the bar impact recovery results here reported only include the loading part. The recovery configuration here reported does not allow calculation of the unloaded part of the stress-strain curve. For this reason, the recovered part of the strain could only be obtained by comparison between the pristine and the recovered sample lengths, as measured by a caliper. After testing, the specimens were coated with 15 nm Au/Pd and imaged in a SEM. It should take into account the fact that the recovery experiments in the present work, especially at high strain rates, were not reported previously. They were performed for understanding energy dissipation mechanisms and revealing the role of microstructure on deformation and failure behavior.

2.6. Statistical analysis

Detection of statistically significant differences (SSD) of the Young's modulus among different orientations were performed by a one-way analysis of variance (ANOVA) method. Tukey's least significant difference procedure was applied to conduct the multiple comparison tests with ANOVA. However, pairwise *t*-test was employed for SSD of Young's modulus between dry and wet condition in each direction as well as strain rate. The statistical significance level for both the ANOVA and *t*-test is assumed 0.05. The mechanical data were collected from multiple specimens in two independent horn samples.

3. Results and discussions

3.1. Hierarchical structure of horn

Fig. 2 shows the tubular structure of the bighorn sheep horn. Curved growth lines were observed from the proximal to distal regions of the horn (Fig. 2a). Previous results reported that the tubules (Fig. 2b) were found to be elliptically-shaped with major axis ~80 μm, and minor axis ~40 μm [20]. HR μ-CT images show the 3D tubular structure (Fig. 2c). Fig. 2d is a cross section along the longitudinal direction, showing that the parallel tubules are continuous along this direction. This is the first 3D study that verifies the tubules are hollow and penetrate, in a short distance, through the horn tissue along the longitudinal growth direction. Since the tubules are produced by epidermal cells, their medullary cells develop at the tip of dermal papillae and subsequently extend through the whole horn [45]. Since the 3D reconstruction of tubules over the entire length of the horn is currently impractical, a sample with a 2 mm length in the base part was selected for micro-CT, which showed continuous tubules over that length. Further studies on tubule continuity in the centimeter length scale will become possible as 3D reconstruction capabilities continue to improve.

Flat, (keratin) cells were identified forming the lamellar structure in the horn. DIC optical microscopy images of the cross section (Fig. 3a) show the cell lamellae surrounding the tubules. Based on the optical microscopy images, the average sizes of the elliptically-shaped cross section of the tubules were calculated. The size of the major axis ranges between 40 – 80 μm with an average of 59 ± 13.8 μm. For the minor axis, the size is in the range of 10 – 40 μm with an average of 24.6 ± 8.9 μm. Both major and minor axes dimensions are similar to what was previously reported [20]. The thickness of each keratin cell is ~1–2 μm. Fig. 3b is a schematic of cell arrangements in a 3D horn model. From the DIC image of the longitudinal section (Fig. 3c), it can be observed that there is an angle (~30°) between the cell lamellae and tubules, which implies that the lamellar cells are not exactly parallel to the tubules. SEM images of the cross section (Fig. 3d) and the longitudinal section (Fig. 3e) further verify the laminated structure around the tubules, also confirming the thickness observed from optical microscopy. Keratin cell surfaces in Fig. 3f show that the cell diameters are ~20–30 μm.

To get further understanding of the lamellar cell size and shape, optical microscopy images of toluidine blue stained thin sections were obtained. The 3D schematic and the optical microscopy images are shown in Fig. 4a and c, respectively, revealed that lamellae have an orientation of 30.16 ± 5.87° (averaged by 18 slices

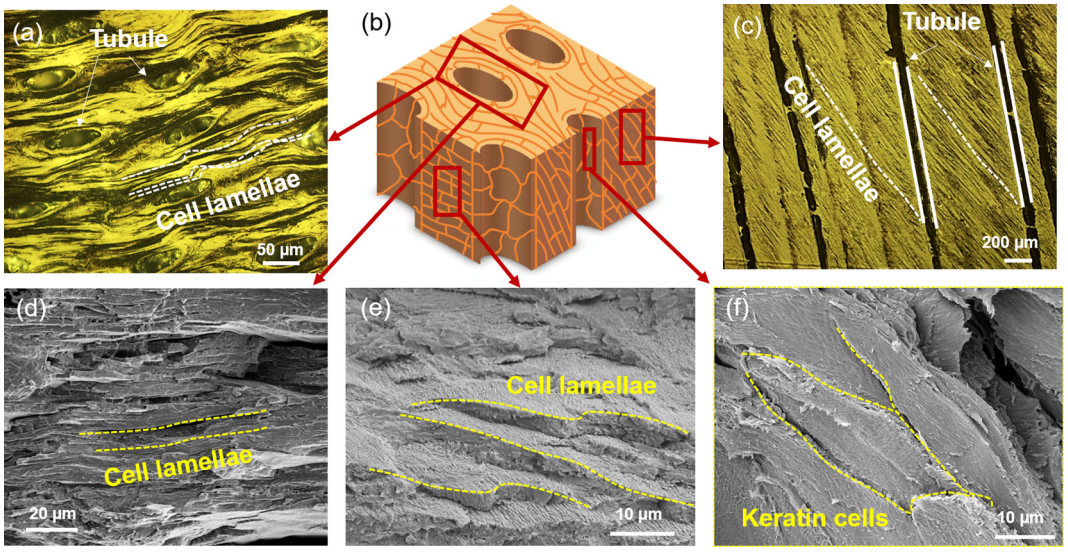

Fig. 3. Tubular and lamellar structure in the bighorn sheep horn: (a) Differential interference contrast (DIC) optical microscopy image of the cross section. Elliptical tubule cross section and curved cell lamellae are observed; (b) Schematic diagram of the tubular and cell lamellar structure; (c) DIC image of the longitudinal section, showing the cell lamellae. The angle between the cell lamella and tubule is ~30°; (d) Scanning electron microscopy image of the cross section. Cell lamellae stacking layer by layer was noticed; (e) Cell lamellae in the longitudinal section shows ~1–2 μm thickness of the lamellae; (f) Keratin cells connect with each other forming the tubules.

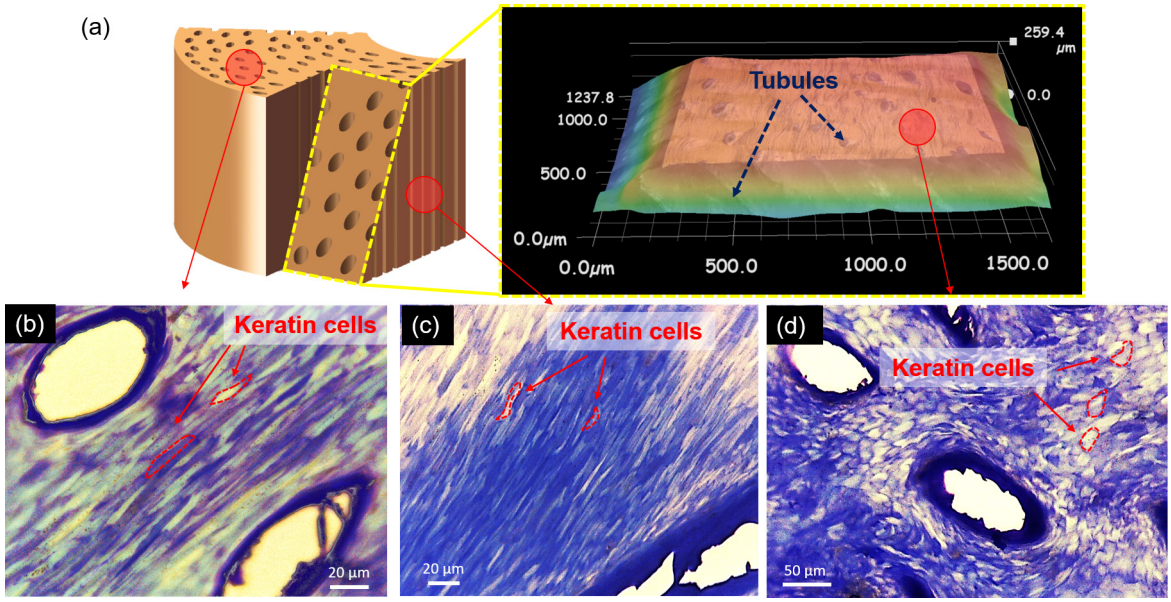

Fig. 4. 3D optical microscopy image of an inclined surface which has ~30° angle with the tubule direction and the keratinous cells arrangement in different surfaces from toluidine blue stained optical microscopy images: (a) The inclined surface in both schematic and 3D optical microscopy image; (b) Toluidine blue stained cross section slice optical microscopy image show the keratin cells along the major axis direction of the ellipse; (c) Needle like keratin cells with thickness ~1–2 μm in the longitudinal section, showing ~30° angle with the tubule edge; (d) Keratin cells in the inclined surface indicating the irregular shapes of keratin cells connected with each other, and having a diameter 20–30 μm.

from six different samples) with respect to the tubule direction. Examining the inclined surface in Fig. 4a reveals the surfaces of the cells. Cross- (Fig. 4b) and longitudinal sections (Fig. 4c) show the flat cells connected with each other forming a layered structure with the same thickness as the thickness of cells, ~2 μm. Fig. 4d shows the cells arranged in the inclined surface, revealing an irregular organization of the flat cells. The average length of the cells is ~20–30 μm, which is more than ten times larger than the thickness. Thus, it can be concluded that the laminated keratinized cells are stacked layer-by-layer in a direction not parallel with the tubules, but at an angle of ~30°.

TEM images of the cross section (Fig. 5a) show parallel cell boundaries, corresponding to the laminated structure observed in both optical and SEM images. Curve-shaped cell membranes are evident (Fig. 5b) revealing the source of surface roughness highlighted in previous work [46]. These rough cell surfaces increase the contact areas between adjacent cells, and result in creation of interlocking interfaces, which lead to higher resistance to delamination between the cell lamellae [46]. Keratin macrofibrils (bundles of IFs) are found inside the cells, with a diameter of ~200 nm. Fig. 5c and d are TEM images of the longitudinal section, showing different orientations of macrofibrils. The fibrils inside the cells are randomly arranged in the cell planes (since the thickness is much smaller than the diameter of cells, the flat cells can be assumed as "planar") (Fig. 5c and d). No fibrils are found perpendicular to the cell plane. Therefore, the mechanical properties of these laminated structures should be transversely isotropic because of the in-plane arrangement of the macrofibrils. Further implications on mechanical properties will be discussed in a later section. The parallel cell boundaries also show a lamellar cell structure in this longitudinal section. IFs, with average diameter of ~12 nm, are observed in the macrofibrils (Fig. 5e).

In summary, the hierarchical structure of bighorn sheep horn from the macro- to nano- scale level is illustrated in Fig. 6. Tubules with elliptical cross section (~59 μm in major axis, ~25 μm in minor axis) are aligned along the horn growth direction. The whole structure is formed by lamellar keratinized cells (20–30 μm in diameter, 1–2 μm in thickness). The laminae are stacked sequentially with a ~30° angle with respect to the tubule direction. Inside the flat keratinized cell, macrofibrils with diameter ~200 nm are distributed in the plane of the cell with a random orientation. At the nano-level, intermediate filaments (IFs, ~12 nm in diameter) embedded in an amorphous keratin matrix are the components of the macrofibrils [10].

3.2. Strain rate, anisotropy and water dependency of mechanical properties

Stress-strain curves obtained for range of quasi-static to dynamic strain rates ($1 \times 10^{-3}\ s^{-1}$ to $4 \times 10^{3}\ s^{-1}$) under uniaxial compression are summarized in Fig. 7. The results for the dried and hydrated specimens compressed along different orientations are plotted in Fig. 7a–c and d–f, respectively. Similar to the mechanical response of polymeric materials, which is significantly influenced by strain rate [47], the stress-strain curves, for all three tested orientations, exhibit a strong rate-dependent behavior. The stiffness, based on the initial slope and the yield stress increase with increasing strain rate. The latter observation is a common phenomenon for polymers and is related to secondary molecular processes [48,49]. However, it has been hypothesized that lack of sufficient time for rearrangement of keratin network, into lower energy configurations, might be another reason of the higher yield stress with increasing rate [20,50]. Table 1 shows the Young's modulus comparison for different strain rate, loading directions, and hydration states. The Young's modulus in the dry state increases 2–3 times when the strain rate changes from $1 \times 10^{-3}\ s^{-1}$ to $4 \times 10^{3}\ s^{-1}$, while it is almost a ten times higher in the hydrated condition. This reveals the importance role of hydration on viscosity characteristics besides the heterogeneous structure in damping the travelling stress waves, which requires further investigations. The data in Table 1 were illustrated in a bar chart (Fig. 8) with further statistical analyses. Significant differences were found between dry and wet samples in all directions and strain rates based on *t*-tests. At lower strain rates $0.001\ s^{-1}$ and $0.1\ s^{-1}$ (Fig. 8a and b), compressive Young's modulus of dry samples reveals negligible difference between longitudinal and transverse

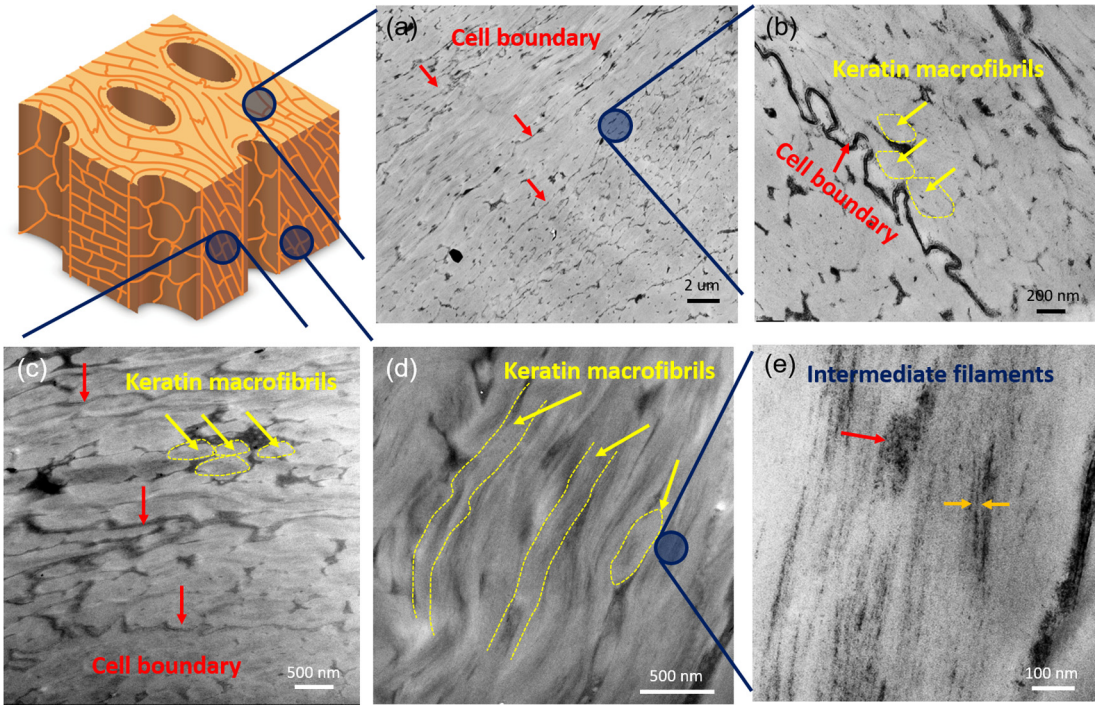

Fig. 5. Transmission electron microscopy images of keratin cell lamellae for different surfaces: (a) Parallel cell boundaries (dark lines, indicated with red arrow) are shown, indicating the cells are stacked layer by layer along the thickness direction; (b) Curved characteristic of cell boundary (dark line) in a higher magnification. Cross section of keratin macrofibres (yellow arrow and circle) exist in the cells, and the diameter of the macrofibril is around 200 nm; (c) Curved cell boundaries are also found in longitudinal section, which is similar as the cross section. Keratin macrofibrils (yellow arrow and circle) cross sections are also indicated here; (d) keratin macrofibrils (yellow arrow and circle) are found parallel with the longitudinal imaging surface; (e) Intermediate filaments in the macrofibrils in a higher magnification. (For interpretation of the references to colour in this figure legend, the reader is referred to the web version of this article.)

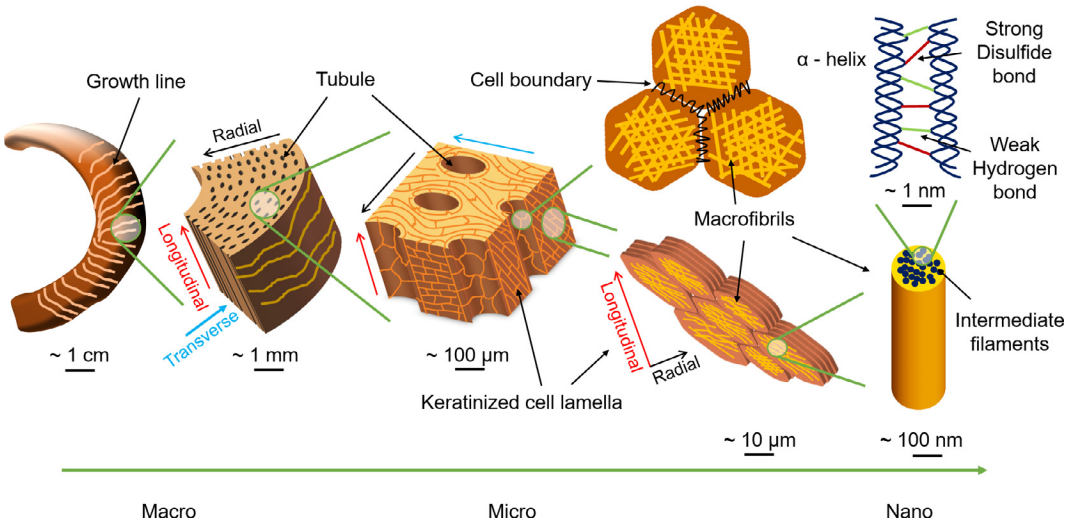

Fig. 6. Hierarchical structure of the bighorn sheep horn: From left to right, curved horn with growth lines from base to the tip at the macro level; Elliptical tubular structures along the growth direction; At the micro level, lamellae of keratinized cells are stacked layer by layer around the tubules, and cell lamellae are oriented ~30° to the tubule direction. Keratinized cells are flat pancake-shaped, with diameters ~20–30 μm and thicknesses ~1–2 μm; At the nano level, each cell contains macrofibrils with a diameter of ~ 200 nm. The macrofibrils are randomly orientated inside the cell plane. The macrofibrils are composted of intermediate filaments with diameter ~12 nm; At the molecular level, intermediate filaments are formed by alpha-helix with hard disulfide bonds and weak hydrogen bonds connected with each other [25].

directions, while they both are significantly higher than the one in the radial direction. However, at higher strain rates (~ 0.5–4000 s^{-1}, Fig. 8c and d), there is no significant difference among the Young's modulus of all the three directions of dry samples. The comparison reveals transverse isotropicity in lower strain rates, which is believed coming from the in-plane arrangement of keratin macrofibrils. Thus, it can be concluded that the keratin macrofibrils can increase the compression stiffness along the fibril direction.

Furthermore, it can be observed from Fig. 7, that a higher strain rate results in greater increase of anisotropic behavior of the dried specimens. The curves for dynamic tests exhibit a linear elastic region up to the yield point. The post-yield behavior is strongly

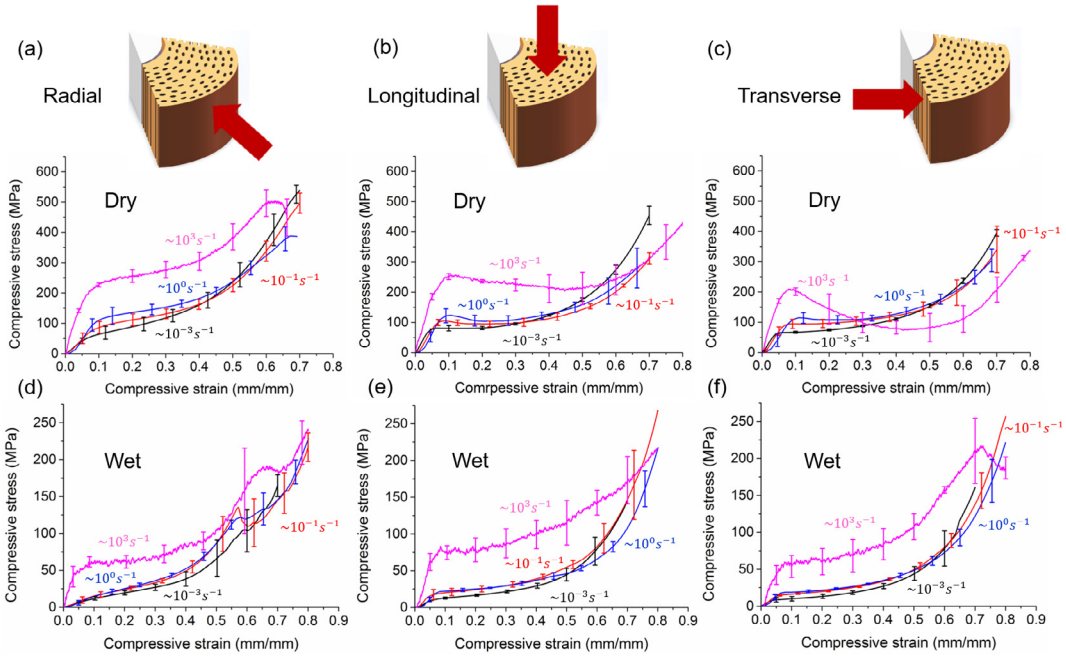

Fig. 7. Stress strain curves of compression tests at different strain rates (from $\sim 10^{-3}$ s^{-1} to 10^{3} s^{-1}), orientations, and hydration states: The top row shows stress-strain curves obtained under dry condition, (a) Radial direction; (b) Longitudinal direction; (c) Transverse direction; Bottom row shows results for the hydrated state, (d) Radial direction; (e) Longitudinal direction; (f) Transverse direction. The stress strain curves are the average values of at least 3 samples.

Table 1
Comparison of Young's modulus at different compressive strain rates, loading directions and hydration states.

Strain rate (s^{-1})	Radial (GPa)		Longitudinal (GPa)		Transverse (GPa)	
	Dry	Wet	Dry	Wet	Dry	Wet
0.001	0.96 ± 0.16	0.13 ± 0.04	1.875 ± 0.17	0.2 ± 0.08	1.75 ± 0.2	0.22 ± 0.08
0.1	1.1 ± 0.2	0.192 ± 0.07	2 ± 0.2	0.4 ± 0.1	1.9 ± 0.22	0.383 ± 0.11
0.5	1.55 ± 0.3	0.207 ± 0.08	2.1 ± 0.22	0.475 ± 0.15	1.96 ± 0.18	0.415 ± 0.12
4000	3.486 ± 0.23	1.433 ± 0.26	3.66 ± 0.25	1.525 ± 0.28	3.58 ± 0.209	1.266 ± 0.26

anisotropic with the degree of softening a function of loading direction. The plot for the radial specimens shows a saddle point with a rising flow stress before ultimate failure. For the longitudinal orientation, a very small softening is observed post-yielding. Conversely, the transverse specimens show a dramatic strain softening up to a local minimum and then a hardening behavior before a catastrophic failure. These kinds of compressive responses were reported for polymeric foams with various densities under dynamic loading [51,52]. Based on the horn microstructure, the quasi-static and impact forces along the radial direction are almost perpendicular (larger than 60°) to the cell surface, which will only densify the keratin cell layers. However, forces in both longitudinal and transverse directions, are nearly perpendicular to the cell thickness direction; thus, leading to buckling and collapse of the laminated structure. To better understand the anisotropic behavior in horn, which is rooted in its structural morphology, bar impact recovery test results are described in the next section.

Similar to the dried tested specimens, there is an increasing trend for stiffness and yield strength from quasi-static loading to high strain rate tests under the hydrated condition. However, the stress-strain curves demonstrate the same overall shape for all tested directions, which implies a much milder anisotropic response in the hydrated state. Thus, the influence of water content is dominant over other factors, such as the microstructural elements. Another important feature that is originated from the dominancy of hydration, is the resiliency compared to the dried specimens. The reduction of stiffness and strength due to the hydration reveals how keratin materials are susceptible to water content and become more compliant. Increasing water content also contributes to changes in viscoelasticity, and subsequent changes in anisotropicity. In this regard, Kitchener [17] studied the effect of water on linear viscoelasticity of horn sheath keratin, which showed more non-linearity of the viscoelastic behavior with increasing hydration.

Although the water content in fresh bighorn sheep horn remains unknown, Kitchener and Vincent [18] reported fresh oryx horn had a water content of 20 wt%. Since both horns are made from crystalline α-keratin embedded in an amorphous keratin matrix, it can be assumed that they have similar range of water content in the fresh status. The *in vivo* condition of 20% hydration is hard to obtain in the laboratory, since partially hydration leads to a nonuniform distribution of water (e.g. a portion of the water may stay inside the tubules), which will cause the inaccurate measurements of the water contents and mechanical properties. Therefore, we aimed to test the dry (∼10%) and fully hydrated (∼30%) samples, which would be the lower and upper limit of the live horn materials. It is worth noting that the energy absorption per unit volume, which can be defined as the area under the stress-strain curves, is higher for the radial direction than the other orientations. Fig. 9 shows the impact energy absorption versus compressive strain in different loading directions and hydration states. This shows that the dry samples absorb more energy than

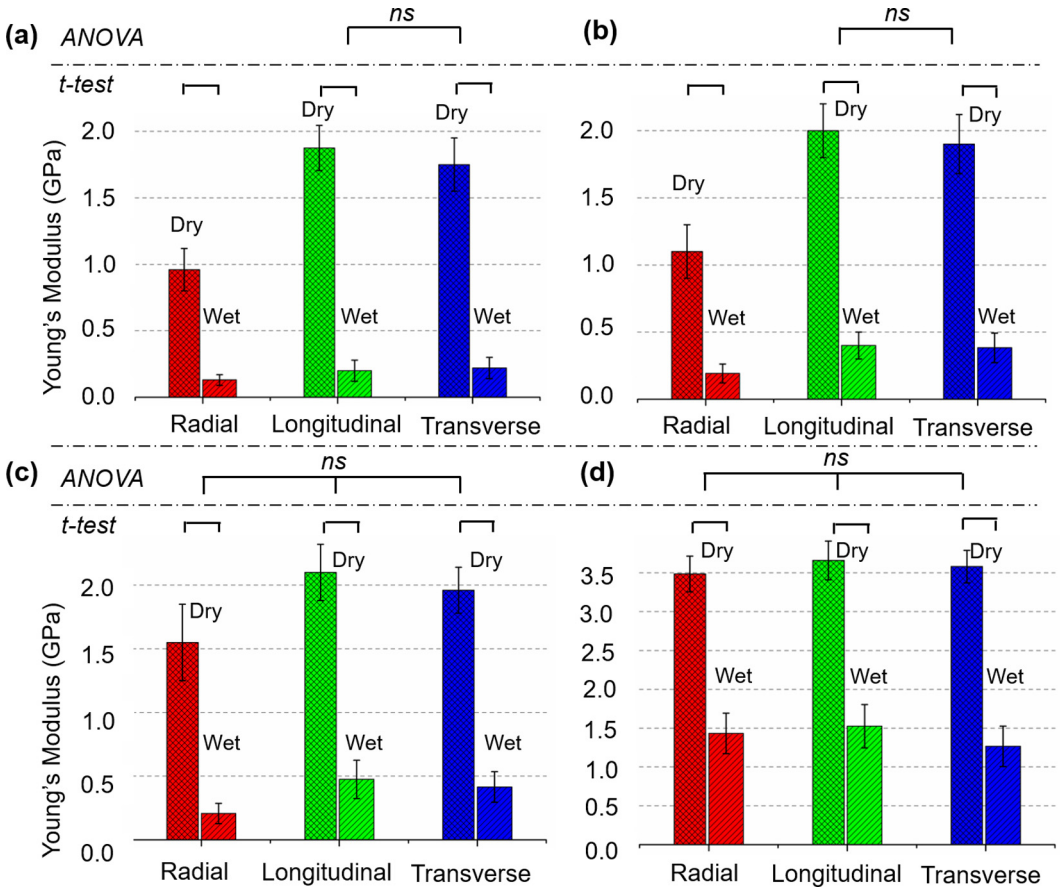

Fig. 8. Bar chart of the Young's modulus of horn samples in different directions, hydration states, and strain rates: (a) strain rate 0.001 s^{-1}; (b) strain rate 0.1 s^{-1}; (c) strain rate 0.5 s^{-1}; (d) strain rate 4000 s^{-1}. *t*-tests between all the dry and wet conditions. One-way ANOVA tests were conducted for the different directions for each strain rate. "ns" refers to negligible statistically significant difference between the results with the level of 0.05.

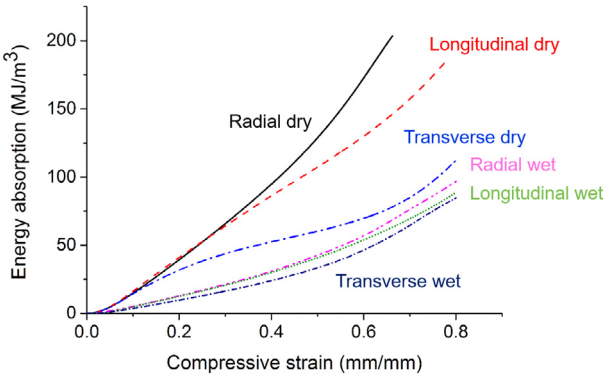

Fig. 9. Impact energy absorption (area under stress-strain curves) as a function of compressive strain in different loading directions and hydration states at a high strain rate ($\sim 10^3$ s^{-1}). The energy absorption data for each condition were averaged from three samples.

the hydrated ones due to the higher initial stiffness and yield strength under dry conditions. Moreover, it is noticeable that the energy absorption has the highest value for the radial direction. Thus, it can be concluded that the radial direction is the main direction of impact resistance in horns. Further understanding of this observation requires a detailed investigation of the tubule distribution along with a correlation of mechanical properties in the three orthogonal directions. It was previously suggested that increasing the tubule density can lead to higher energy absorption capability [53]. Analysis of these features will be conducted in future studies.

3.3. Hopkinson bar impact recovery test results and failure mechanisms

Fig. 10 corresponds to the Hopkinson bar impact recovery tests along with images of sample surfaces before and after testing for the dried specimens. The loading-unloading curves for quasi-static tests show a similar linear elastic region behavior with a plateau for longitudinal and transversal directions, and an increasing stress flow for the radial direction (Fig. 10a–c). In all directions, the specimens maintained a residual deformation after unloading, even though the elastic portion of the strain was recovered. In the case of dynamic loading, the elastic recovery was obtained by comparing the pristine length of specimen with the deformed length after dynamic loading (labeled as 'f' on Fig. 10a–c).

Comparing the pristine surfaces (Fig. 10d–f) with the deformed ones (Fig. 10 g–l) reveals the role of tubules in microstructural damage mechanisms. In this regard, the macroscopic observations are discussed first, and then more detailed deformation mechanisms are reported. Optical microscopy images of deformed surfaces were acquired after quasi-static compression (Fig. 10 g–i), while scanning electron microscopy images (Fig. 10j–l) were taken from the dynamic compression because of the severely deformed and uneven surface, which made it hard to visualize using optical microscope. For the radial direction, the load was applied parallel to the minor axis of the elliptically-shaped tubules. Under quasi-static loading, tubule distortion with increases in major and

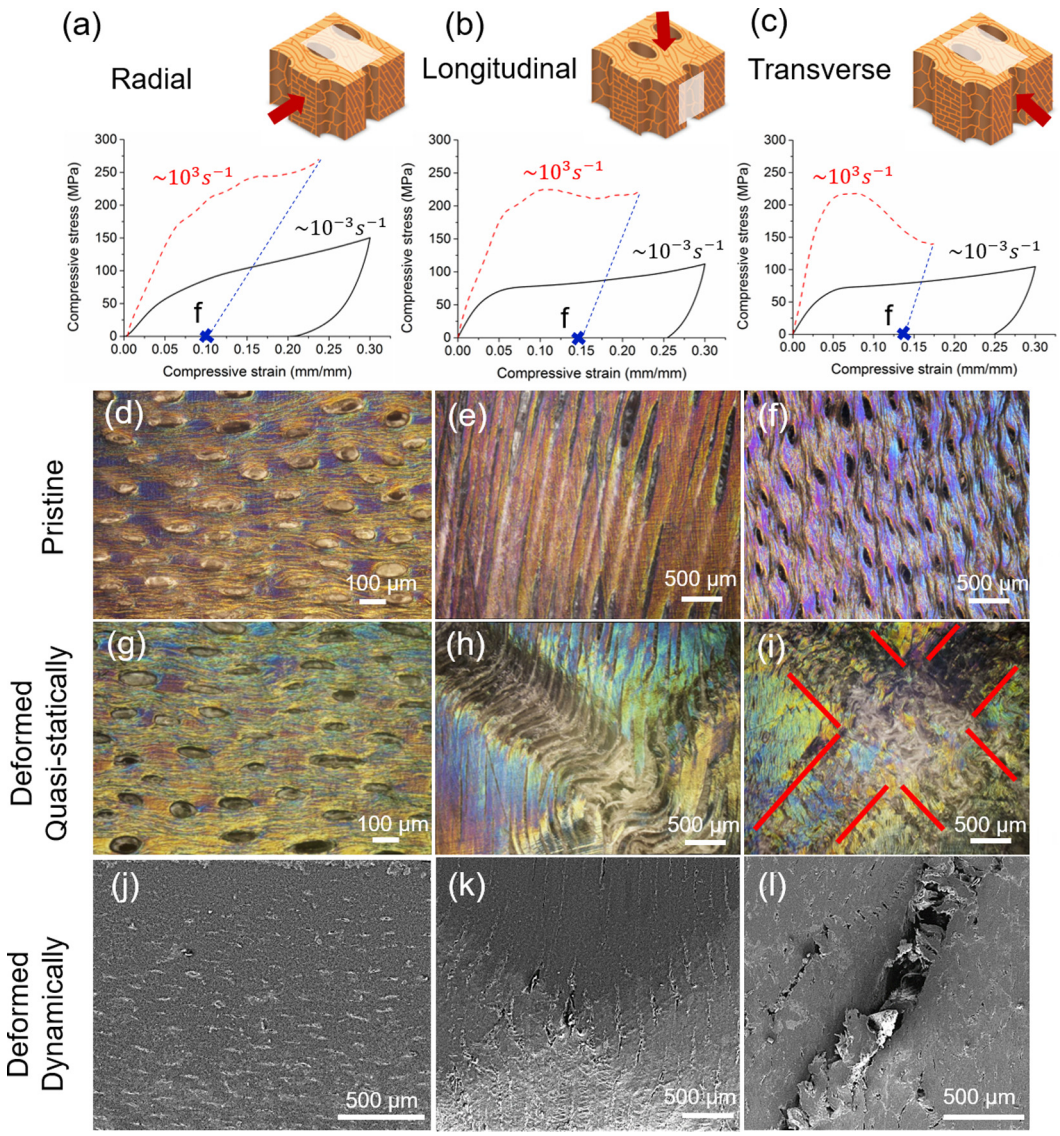

Fig. 10. Bar impact recovery compression tests performed on dry samples under compression: (a–c) Stress-strain curves with loading and unloading under quasi-static (solid lines, strain rate 10^{-3} s^{-1}) and dynamic loading conditions (dashed lines, strain rate 10^{3} s^{-1}) along the radial, longitudinal, and transverse directions; f in the plots correspond to the final states in the dynamic tests, showing significant residual strains after recovery tests; (d–f) Differential interference contrast optical images of pristine surfaces in different directions: radial, longitudinal, and transverse, respectively; (g–i) Surfaces in three directions after 30% quasi-static deformation; buckled and kinked lamellae formed shear bands in h; X-shaped shear bands indicated with red lines in i; (j–l) Scanning electron microscopy images of the sample surfaces in the three directions after ~20% impact deformation (strain rate ~10^{3} s^{-1}).

decreases in minor axis dimensions are observed (Fig. 10g) when compared with the pristine sample (Fig. 10d); under dynamic loading more pronounced changes are observed with most of the tubules collapsed (Fig. 10j). In the longitudinal direction when the load is applied parallel to tubules, buckling of lamellae is noticeable under both quasi-static (Fig. 10h) and dynamic loading (Fig. 10k) conditions. In this case, layers of buckled or kinked lamellae form a shear band. Under quasi-static loading along the major axis of the tubules (transverse direction), most of the tubules collapse and cause localized inelastic deformation with X-shaped shear bands (Fig. 10i). This deformation mode mostly controls plasticity and failure, and is very common in heterogeneous and amorphous material systems [54]. More severe deformation occurs for the dynamic loading in the transverse direction. Fig. 10l shows that several microcracks formed with a macrocrack propagating diagonally. The specimen exhibited a shear-type failure along the direction of maximum shear stress followed by delamination. This could explain the strongest strain softening measured in this direction compared to the other directions.

Images of hydrated samples, recovered after ~30% strain are given in Fig. 11. In contrast to the dried specimens, most of the strain is recovered under both quasi-static and dynamic loading (Fig. 11a–c). The residual quasi-static strain is obtained from the unloading data, while the residual dynamic strain is extracted by the comparison between the initial length (i.e. before tests) of the specimen and the final one (i.e. after tests). In this regard, there is ~5% remaining strain under quasi-static compression, but negligible residual strain under high strain rate impact in all directions based on the measured lengths under loads before and after the tests. Fig. 11d–f show the optical microscopy image of the original surface in radial, longitudinal, and transverse direction respectively. Water drops were squeezed out under quasi-static compression in radial direction (Fig. 11g). Slight lamella buckling was noticed after quasi-static compression in longitudinal direction

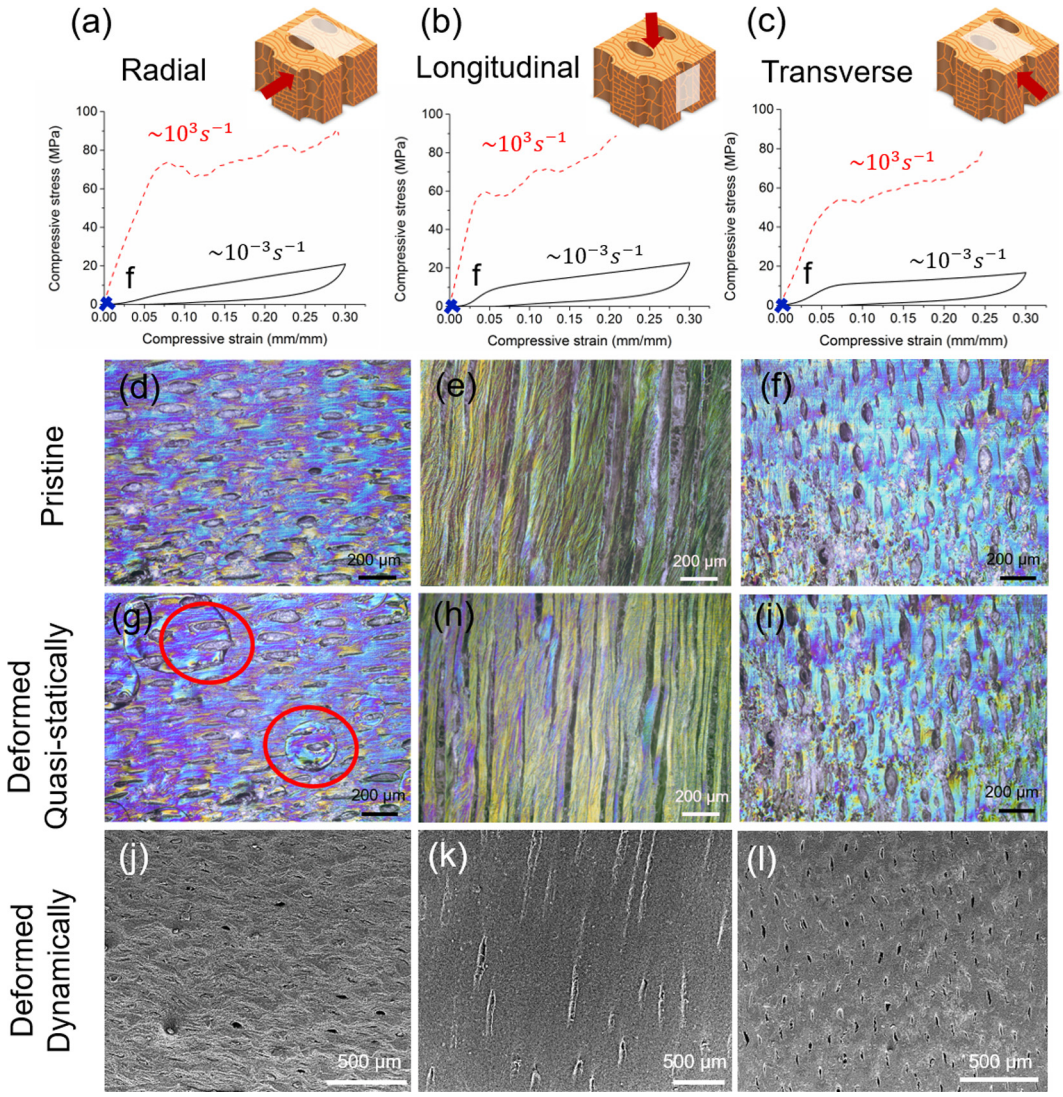

Fig. 11. Bar impact recovery compressive tests of hydrated samples under compression: (a–c) Stress-strain curves with loading and unloading under quasi-static (solid lines) and impact loading conditions, the latter with limited strain (~30% strain, dashed lines) along radial, longitudinal, and transverse directions, respectively; f in the plots correspond to the final states in both quasi-static and dynamic tests, indicating almost no residual strain after recovery tests; (d–f) Differential interference contrast optical images of original surfaces before compression in different directions: radial, longitudinal and transverse, respectively; (g–i) Surfaces in three directions after 30% quasi-static deformation. Red circles in (g) indicate water drops squeezed out after radial compression; (j–l) Scanning electron microscopy images of the surfaces in three directions after ~30% impact deformation.

(Fig. 11h). SEM images of surfaces in different directions when subjected to high strain rates are shown in Fig. 11j–l. In contrast to the dried tested specimens, no distinguishable damage in the hydrated tests can be observed. This can be explained by the hydration dependence of the glass transition temperature of keratin materials. The glass transition temperature of human hair and wool decreases from ~80 °C (~10% water content) to ~20 °C (~20% water content) because of the plasticizing effects of water on the keratin matrix [55]. It is well established that the keratinous microfibrils in wool, hair, horn, and hoof possess similar dimensions, with low-sulfur proteins arranged in the same manner [56]. However, horn keratin contains a smaller proportion of matrix than hair and wool [56–58]. Therefore, horn keratin is expected to experience a reduction in glass transition temperature after hydration but of lower degree compared with the ones observed for hair and wool. The wet horn samples have ~30% water content, indicating both the quasi-static and dynamic compression tests occur around the glass transition temperature, leading to elastomer-like stress strain curves. This is why no residual strains and distinguishable damage occur in totally hydrated samples, while the dry samples show brittle failure. Deformation recovery in animal hairs, in the hydrated state, was also identified in previous work. The explanation was that presence of water molecules in the keratin matrix allows breakage and reformation of hydrogen bonds, which along with the higher flexibility of macromolecular chains made deformation recovery possible [59]. Since the horn material here studied possesses a similar keratin matrix composition and structure, we infer that the recovery behaviors found in fully hydrated horn samples can be explained by the effect of water on the keratin matrix. In addition to this, we hypothesize that the hollow tubules inside the horns may increase the water absorption, thus further assisting the recovery of horn tissues after impact. This hypothesis will be explored in future studies.

More detailed compressive deformation mechanisms are summarized in Fig. 12. Deformed tubules in the radial direction are shown in Fig. 12a–d. In the dry state, tubules are relatively distorted along both major and minor axes under quasi-static load

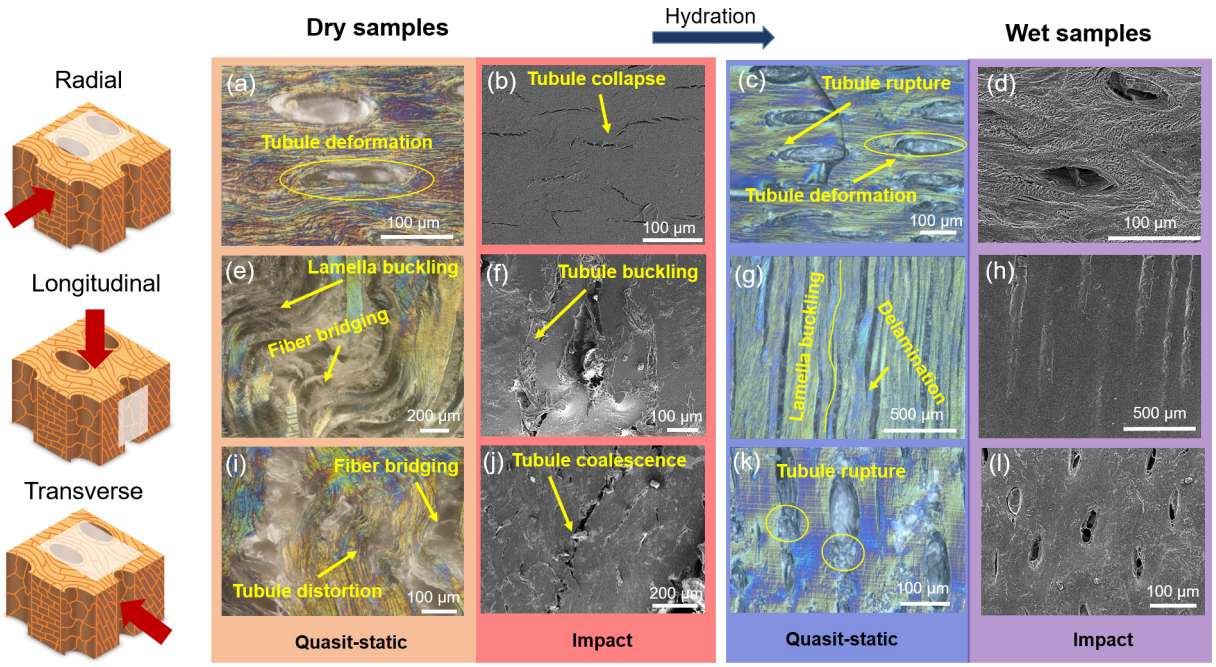

Fig. 12. Detailed failure mechanisms under different loading directions, rates (quasi-static $\sim 10^{-3}\ s^{-1}$ and impact $\sim 10^{3}\ s^{-1}$), and hydration states (dry and hydrated). Quasi-statically loaded samples were imaged in an optical microscope while dynamically loaded samples were imaged using a scanning electron microscopy. Each row of images correspond to radial (a–d), longitudinal (e–h), and transverse (i–l) directions, respectively: (a) Tubule deformed under quasi-static compression in the radial direction; (b) Tubule collapse under high strain rate impact in the radial direction; (c) Tubule tearing at the corner and slightly deformed in the hydrated condition; (d) no obvious failure under impact for wet samples; (e) Lamella buckling, kinking, and fiber bridging under quasi-static compression in the longitudinal direction; (f) Tubule buckling under impact in longitudinal direction; (g) Lamellae buckling and delamination in hydrated samples under quasi-static compression in longitudinal direction; (h) no obvious damage under impact in longitudinal direction; (i) Tubule distortion and fiber bridging in dry samples under quasi-static compression; (j) Tubule coalescence under impact in transverse direction; (k) Tubule rupture in wet samples under quasi-static compression; (l) no obvious damage in wet samples under impact in transverse direction.

(Fig. 12a). Under dynamic loading, the tubules compressed significantly and separated into small cavities, and also deform from elliptical shapes to crescent shapes with opposite concavities or in some cases complete flattened shapes (Fig. 12b). This can stem from the perpendicular deviation of the loading direction respect to the major axis of the tubule due to the non-uniform radially distributed tubules (see Fig. 2c), which led to the development of homogenous and heterogeneous flattening with different concavities. For the quasi-static hydrated case, absorption of water seems to lead to stress concentration at the vertices of the ellipses. This is noticeable from some damage accumulation at those vertices as observed after the tests (Fig. 12c). However, no significant deformation is found under impact loading for the hydrated samples (Fig. 12d). This is consistent with the bar impact recovery test result, where deformation was fully recovered. Longitudinally deformed surfaces in dry condition indicate lamellae buckling and kinking along with fiber bridging (Fig. 12e–f). Interestingly, buckled lamellae show two opposite curvatures, which surrounded an accumulated damage zone. Slight lamellae buckling and delamination is noticed in hydrated samples under longitudinal loading (Fig. 12g). Fig. 12h is the longitudinal surface of the hydrated samples after dynamic compression. Compared with the dry surface (Fig. 12f), no damage is observed. Finally, distortion and rupture of the tubules are noticeable for the transversal direction. Fig. 12i shows tubule distortion and fiber bridging in dry samples under quasi-static compression. However, the image for the dried specimen under dynamic loading demonstrates how a microcrack forms. In this case, similar to the radial direction, tubules adopt crescent shapes and coalescence of them is the source of nucleation sites for cracks (Fig. 12j). Rupture of tubules also occurs in the hydrated samples in the transverse direction (Fig. 12k). No evident failure mechanism is observed for the hydrated samples under dynamic loading in all directions (Fig. 12d, h, l). Fig. 12 summarizes the failure mechanisms in different loading orientations, loading strain rates, and hydration states, which gives an effective explanation of the stress strain curves shown and described in Section 3.2. Future work will investigate recovery mechanisms of hydrated samples and its relevance to bioinspired designs. The various energy dissipation mechanisms found here could give inspiration on synthesis of multiscale laminated composites with incorporation of tubule for crashworthiness application. In the event of dynamic collision or accident, structures are conventionally made of ductile metals to absorb the crash energy; however, manufacturing viscoelastic composite with the inspired microstructure revealed by the present study may improve energy absorption capacity along with a light-weight design. In this regard, a parametric study and analysis of the interplay between material parameters and microstructural features is essential for design of optimum synthetic material performance.

4. Conclusions

The structure, quasi-static and dynamic mechanical properties and damage mechanisms of a bighorn sheep (*Ovis canadensis*) horn were investigated. The structure was examined by optical, scanning and transmission electron microscopy along with high resolution micro-computed tomography. High strain rate dynamic compression was performed by a Hopkinson bar and results were compared to quasi-static compression experiments. Different compressive deformation mechanisms during testing were observed and summarized in Section 3.3. The reason why bighorn sheep horn can withstand blows during ramming are: 1) the radial direction (impact direction) was found to have the highest strength and

energy absorption in both dry and hydrated states; 2) The deformation recovery exhibited by horns in the hydrated states appear to confirm them the ability to withstand multiple blows without fracture during ramming. As a result, the main conclusions in present work are:

- The horn microstructure consists of tubules as well as a laminated structure formed by keratinous cells. The former are located along the longitudinal direction with an elliptically-shaped cross section (major axis ~59 μm, minor axis ~25 μm), confirmed by high resolution X-ray computed tomography. Laminated keratinous cells surround the tubules. The dimension of the keratin cells are 20–30 μm in diameter and 1–2 μm in thickness. There is a ~30.16 ± 5.87° angle between cell lamellae and tubules.
- Keratin macrofibrils with diameter ~200 nm were found randomly oriented in the keratinized cell planes and parallel with the cell surfaces. The fibrils are bundles of intermediate filaments with dimension ~12 nm in diameter. These in-plane arrangements of macrofirbils, reported here for the first time, explain the transverse isotropic behavior identified through compression tests.
- Stress strain curves of quasi-static and dynamic tests indicated higher energy absorption and impact resistance in the radial direction, which is the impact direction of the horn. Initial Young's modulus of dry samples in longitudinal and transverse directions are significant higher than in the radial direction at lower strain rates (0.001 and 0.1 s^{-1}), showing transverse isotropy due to the laminated structure around the tubules.
- Damage at various strain rates was examined by conducting Hopkinson bar impact recovery tests. More material damage is observed with increasing strain rate in the dry condition. Pre- and post-test microscopy imaging reveals various inelastic deformation mechanisms: kink bands, lamella buckling, tubule collapse, and microcracking, which highlighted the role of structural elements such as tubules and lamellae in relation to loading. Tubule collapse in the radial direction leads to significant energy absorption, while lamella buckling and shear band formation in the longitudinal and transverse directions cause catastrophic failure of material with less energy absorption.
- Dramatic differences in behavior were observed as a function of sample hydration. Under the dry condition, the samples exhibited a strong anisotropic behavior as well as strain rate dependency. Specimen hydration leads to a more isotropic behavior, while still rate dependent. The hydrated specimens recover their initial length under dynamic loading at strains as high as 20–30%. This can be explained by the decrease of the glass transition temperature of hydrate samples, thus leading to a strong viscoelastic behavior under compression. This feature is remarkable because it shows that hydrated horn material can absorb significant amounts of energy without damage.

The findings of this study demonstrated how horn dissipates large amount of energy during deformation in different orientations and hydration states. Moreover, the revealed hierarchical organization of horn constituents such as layers of keratin cells along with incorporation of tubules can serve as bio-inspiration for the design of synthetic composites. Compression tests in dry conditions demonstrate the role of tubules in the deformation mechanisms as well as their role in determining the preferable impact orientation. Therefore, the results of this paper hint at a path to tune energy-absorbent engineering materials that incorporate tubular structures as a function of impact direction. Moreover, the water-assisted recoverability of keratin under high-energy impact provides inspiration towards design of recoverable energy-absorbent materials.

Acknowledgements

This work is supported by a Multi-University Research Initiative (MURI) through the Air Force Office of Scientific Research of the United States (AFOSR-FA9550-15-1-0009) and a National Science Foundation Biomaterials Program Grant 1507978. We appreciate Eric Bushong and Mason Mackey at National Center for Microscopy and Imaging Research (NCMIR), Timo Meerloo and Ying Jones at Electron Microscopy Facility at UC San Diego for providing the help with micro-computed tomography and TEM sample preparation and imaging. We thank Ryan Anderson of the Nano3 Laboratory of CalIt2 for helping with the SEM and optical microscopy and Prof. Marc A. Meyers from UC San Diego for his kind and enthusiastic support of this project. This work was performed in part at the San Diego Nanotechnology Infrastructure (SDNI) of UCSD, a member of the National Nanotechnology Coordinated Infrastructure, which is supported by the National Science Foundation (Grant ECCS-1542148).

References

[1] U.G.K. Wegst, M.F. Ashby, The mechanical efficiency of natural materials, Phil. Mag. 84 (2004) 2167–2181.
[2] A. Kitchener, An analysis of the forces of fighting of the blackbuck (antilope-cervicapra) and the bighorn sheep (*Ovis-Canadensis*) and the mechanical design of the horns of bovids, J. Zool. 214 (1988) 1–20.
[3] Courtney M, Courtney A, "Sheep Collisions: the Good, the Bad, and the TBI," arXiv preprint arXiv:0711.3804, (2007).
[4] V. Geist, The evolution of horn-like organs, Behaviour 27 (1966) 175–214.
[5] A. Drake, T.L.H. Donahue, M. Stansloski, K. Fox, B.B. Wheatley, S.W. Donahue, Horn and horn core trabecular bone of bighorn sheep rams absorbs impact energy and reduces brain cavity accelerations during high impact ramming of the skull, Acta Biomater. 44 (2016) 41–50.
[6] Domenici P, Blake, R.W., "Biomechanics in Animal Behavior," (BIOS Scientific, 2000).
[7] Rayner JMV, Wootton RJ, Society for Experimental Biology (Great Britain), Biomechanics in evolution. Society for Experimental Biology seminar series (Cambridge University Press, Cambridge; New York, 1991), pp. xiv, 273 pages.
[8] A. Kitchener, The effect of behavior and body-weight on the mechanical design of horns, J. Zool. 205 (1985) 191–203.
[9] Blake RW, Domenici P, Biomechanics in animal behaviour. Experimental biology reviews (BIOS Scientific, Oxford, 2000), pp. xv, 344 pages.
[10] B. Wang, W. Yang, J. McKittrick, M.A. Meyers, Keratin: Structure, mechanical properties, occurrence in biological organisms, and efforts at bioinspiration, Prog. Mater Sci. 76 (2016) 229–318.
[11] J. McKittrick, P.Y. Chen, S.G. Bodde, W. Yang, E.E. Novitskaya, M.A. Meyers, The structure, functions, and mechanical properties of keratin, JOM 64 (2012) 449–468.
[12] R. Fraser, T. MacRae, A. Miller, The coiled-coil model of α-keratin structure, J. Mol. Biol. 10 (1964) 147IN128–156IN129.
[13] R. Marshall, D.-G. Orwin, J. Gillespie, Structure and biochemistry of mammalian hard keratin, Electron. Microscopy Rev. 4 (1991) 47–83.
[14] R. Fraser, T. MacRae, E. Suzuki, Structure of the α-keratin microfibril, J. Mol. Biol. 108 (1976) 435–452.
[15] A.N. Parbhu, W.G. Bryson, R. Lal, Disulfide bonds in the outer layer of keratin fibers confer higher mechanical rigidity: correlative nano-indentation and elasticity measurement with an AFM, Biochemistry 38 (1999) 11755–11761.
[16] D.S. Fudge, K.H. Gardner, V.T. Forsyth, C. Riekel, J.M. Gosline, The mechanical properties of hydrated intermediate filaments: insights from hagfish slime threads, Biophys. J . 85 (2003) 2015–2027.
[17] A. Kitchener, Effect of water on the linear viscoelasticity of horn sheath keratin, J. Mater. Sci. Lett. 6 (1987) 321–322.
[18] A. Kitchener, J.F.V. Vincent, Composite theory and the effect of water on the stiffness of horn keratin, J. Mater. Sci. 22 (1987) 1385–1389.
[19] B.W. Li, H.P. Zhao, X.Q. Feng, W.W. Guo, S.C. Shan, Experimental study on the mechanical properties of the horn sheaths from cattle, J. Exp. Biol. 213 (2010) 479–486.
[20] L. Tombolato, E.E. Novitskaya, P.Y. Chen, F.A. Sheppard, J. McKittrick, Microstructure, elastic properties and deformation mechanisms of horn keratin, Acta Biomater. 6 (2010) 319–330.
[21] M.W. Trim, M.F. Horstemeyer, H. Rhee, H. El Kadiri, L.N. Williams, J. Liao, K.B. Walters, J. McKittrick, S.J. Park, The effects of water and microstructure on the mechanical properties of bighorn sheep (*Ovis canadensis*) horn keratin, Acta Biomater. 7 (2011) 1228–1240.
[22] K. Johnson, M. Trim, D. Francis, W. Whittington, J. Miller, C. Bennett, M. Horstemeyer, Moisture, anisotropy, stress state, and strain rate effects on bighorn sheep horn keratin mechanical properties, Acta Biomater. 48 (2017) 300–308.
[23] A. Kitchener, Fracture-toughness of horns and a reinterpretation of the horning behavior of bovids, J. Zool. 213 (1987) 621–639.

[24] L. Farran, A.R. Ennos, S.J. Eichhorn, The effect of humidity on the fracture properties of human fingernails, J. Exp. Biol. 211 (2008) 3677–3681.
[25] Feughelman M, Mechanical properties and structure of alpha-keratin fibres: wool, human hair and related fibres. (UNSW press, 1997).
[26] A.M. Taylor, R.H.C. Bonser, J.W. Farrent, The influence of hydration on the tensile and compressive properties of avian keratinous tissues, J. Mater. Sci. 39 (2004) 939–942.
[27] J.E.A. Bertram, J.M. Gosline, Functional design of horse hoof keratin – the modulation of mechanical-properties through hydration effects, J. Exp. Biol. 130 (1987) 121–136.
[28] M. Feughelman, M. Robinson, The relationship between some mechanical properties of single wool fibers and relative humidity, Textile Res. J. 37 (1967) 441–446.
[29] M. Breuer, The binding of small molecules to hair-I: the hydration of hair and the effect of water on the mechanical properties of hair, J. Soc. Cosmet. Chem. 23 (1972).
[30] Q.B. Zhang, C. Li, Y.T. Pan, G.H. Shan, P. Cao, J. He, Z.S. Lin, N.J. Ao, Y.X. Huang, Microstructure and mechanical properties of horns derived from three domestic bovines, Mater. Sci. Eng. C 33 (2013) 5036–5043.
[31] M.A. Kasapi, J.M. Gosline, Design complexity and fracture control in the equine hoof wall, J. Exp. Biol. 200 (1997) 1639–1659.
[32] M.A. Kasapi, J.M. Gosline, Micromechanics of the equine hoof wall: optimizing crack control and material stiffness through modulation of the properties of keratin, J. Exp. Biol. 202 (1999) 377–391.
[33] G.T. Gray III, Classic split-Hopkinson pressure bar testing, in: ASM Handbook, Mechanical Testing and Evaluation, 2000, pp. 462–476.
[34] Meyers M, Shock waves and high-strain-rate phenomena in metals: concepts and applications. (Springer Science & Business Media, 2012).
[35] W.N. Chen, G. Ravichandran, Dynamic compressive failure of a glass ceramic under lateral confinement, J. Mech. Phys. Solids 45 (1997) 1303–1328.
[36] F. Rietsch, B. Bouette, The compression yield behavior of polycarbonate over a wide-range of strain rates and temperatures, Eur. Polymer J. 26 (1990) 1071–1075.
[37] J. Richeton, S. Ahzi, K.S. Vecchio, F.C. Jiang, R.R. Adharapurapu, Influence of temperature and strain rate on the mechanical behavior of three amorphous polymers: Characterization and modeling of the compressive yield stress, Int. J. Solids Struct. 43 (2006) 2318–2335.
[38] A. Gilat, R.K. Goldberg, G.D. Roberts, Experimental study of strain-rate-dependent behavior of carbon/epoxy composite, Compos. Sci. Technol. 62 (2002) 1469–1476.
[39] B. Song, W.N. Chen, T. Weerasooriya, Quasi-static and dynamic compressive behaviors of a S-2 glass/SC15 composite, J. Compos. Mater. 37 (2003) 1723–1743.
[40] W. Chen, B. Zhang, M.J. Forrestal, A split Hopkinson bar technique for low-impedance materials, Exp. Mech. 39 (1999) 81–85.
[41] J.M. Yuan, J. Ma, G.E.B. Tan, Specimen stress equilibrium in split hopkinson pressure bar tests of ceramics at high strain rate, Mech. Prop. Perform. Eng. Ceram. Compos. Vi 32 (2011) 55–66.
[42] Chen WW, Song B, Split Hopkinson (Kolsky) bar: design, testing and applications. (Springer Science & Business Media, 2010).
[43] I.M. Daniel, J.M. Cho, B.T. Werner, Characterization and modeling of stain-rate-dependent behavior of polymeric foams, Composites Part A 45 (2013) 70–78.
[44] B. Song, W. Chen, Dynamic compressive response and failure behavior of an epoxy syntactic foam, J. Compos. Mater. 38 (2004) 915–936.
[45] K.D. Budras, C. Schiel, C. Mülling, Horn tubules of the white line: an insufficient barrier against ascending bacterial invasion, Equine Vet. Educ. 10 (1998) 11–15.
[46] B. Wang, W. Yang, V.R. Sherman, M.A. Meyers, Pangolin armor: overlapping, structure, and mechanical properties of the keratinous scales, Acta Biomater. 41 (2016) 60–74.
[47] S.M. Walley, J.E. Field, P.H. Pope, N.A. Safford, A study of the rapid deformation-behavior of a range of polymers, Philos. Trans. R. Soc. A Math. Phys. Eng. Sci. 328 (1989) 1–33.
[48] L.P. Chen, A.F. Yee, E.J. Moskala, The molecular basis for the relationship between the secondary relaxation and mechanical properties of a series of polyester copolymer glasses, Macromolecules 32 (1999) 5944–5955.
[49] J. Richeton, S. Ahzi, L. Daridon, Y. Remond, A formulation of the cooperative model for the yield stress of amorphous polymers for a wide range of strain rates and temperatures, Polymer 46 (2005) 6035–6043.
[50] J.F. Vincent, Structural Biomaterials, Princeton University Press, 2012.
[51] B. Song, W.Y. Lu, C.J. Syn, W.N. Chen, The effects of strain rate, density, and temperature on the mechanical properties of polymethylene diisocyanate (PMDI)-based rigid polyurethane foams during compression, J. Mater. Sci. 44 (2009) 351–357.
[52] W. Chen, F. Lu, N. Winfree, High-strain-rate compressive behavior of a rigid polyurethane foam with various densities, Exp. Mech. 42 (2002) 65–73.
[53] J. McKittrick, P.-Y. Chen, L. Tombolato, E. Novitskaya, M. Trim, G. Hirata, E. Olevsky, M. Horstemeyer, M. Meyers, Energy absorbent natural materials and bioinspired design strategies: a review, Mater. Sci. Eng. C 30 (2010) 331–342.
[54] A.L. Greer, Y.Q. Cheng, E. Ma, Shear bands in metallic glasses, Mater. Sci. Eng. R-Rep. 74 (2013) 71–132.
[55] F.J. Wortmann, M. Stapels, R. Elliott, L. Chandra, The effect of water on the glass transition of human hair, Biopolymers 81 (2006) 371–375.
[56] J.M. Gillespie, A.S. Inglis, A comparative study of high-sulphur proteins from alpha-keratins, Comp. Biochem. Physiol. 15 (1965) 175–182.
[57] R.C. Marshall, J. Gillespie, The keratin proteins of wool, horn and hoof from sheep, Aust. J. Biol. Sci. 30 (1977) 389–400.
[58] H. Edwards, D. Hunt, M. Sibley, FT-Raman spectroscopic study of keratotic materials: horn, hoof and tortoiseshell, Spectrochim. Acta Part A Mol. Biomol. Spectrosc. 54 (1998) 745–757.
[59] Z. Liu, D. Jiao, Z. Zhang, Remarkable shape memory effect of a natural biopolymer in aqueous environment, Biomaterials 65 (2015) 13–21.